JACS
JOURNAL OF THE AMERICAN CHEMICAL SOCIETY
pubs.acs.org/JACS
Article

Manganese Oxide-Incorporated Hybrid Lipid Nanoparticles Amplify the Potency of mRNA Vaccine via Oxygen Generation and STING Activation

Jinqun Gan, Jiaqi Lei, Yongcan Li, Meixin Lu, Xinyang Yu, and Guocan Yu*

Cite This: J. Am. Chem. Soc. 2024, 146, 32689−32700
Read Online

ABSTRACT: Messenger RNA (mRNA) vaccines have exhibited enormous potential in the treatment of human diseases; however, their widespread applications are curtailed by the induction of reactive oxygen species during mRNA translation, which greatly compromises the translation efficiency. Herein, we present a robust strategy with the capability to substantially enhance the efficacy of the mRNA vaccine through promoting mRNA translation and stimulator of interferon genes (STING) activation. The strategy entails the coassembly of small-sized manganese oxide nanoparticles (Mn_3O_4 NPs) with lipid nanoparticles (LNPs) as the hybrid delivery vehicle (MnLNPs) for the fabrication of mRNA vaccine. The acquired MnLNPs proficiently scavenge reactive oxygen species (ROS) produced during mRNA translation and facilitate oxygen production, thereby boosting adenosine triphosphate (ATP) synthesis and augmenting mRNA translation. Furthermore, MnLNPs effectively bolster the antigen presentation and maturation of dendritic cells by activating the cGAS-STING pathway. *In vivo* studies demonstrate that mRNA vaccine prepared from MnLNPs markedly enhances the translation of antigen-encoding mRNA compared to LNPs, leading to superior antitumor efficacy. The tumor-suppressive capabilities of MnLNPs@mRNA are further promoted by synergizing with immune checkpoint blockade, underscoring MnLNPs-based mRNA vaccine as an exceptionally promising avenue in cancer immunotherapy.

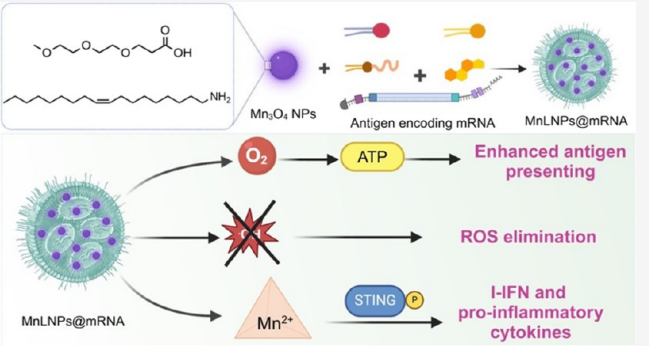

INTRODUCTION

Featuring rapid development cycles and customizable designs, mRNA vaccines have demonstrated exceptional effectiveness ranging from influenza prevention to cancer therapy.[1−10] However, a critical limitation hindering the full potential of lipid nanoparticles (LNPs)-based mRNA vaccines is the suboptimal mRNA translation efficiency that diminishes their ability to activate the immune system, arising from the reactive oxygen species (ROS) generated during mRNA translation.[11−13] ROS, comprising various oxygen derivatives, such as hydrogen peroxide (H_2O_2) and hydroxyl radicals ($^{\bullet}OH$), are crucial for maintaining normal physiological functions and play key roles in cell signaling and immune responses.[14−17] However, their overproduction and accumulation, instigated by external factors like mRNA transfection, not only induces oxidative stress leading to cellular impairment but also triggers the hypoxia response pathway, which in turn inhibits cellular metabolic activities and diminishes the translation efficiency of mRNA.[18,19]

Another practical challenge impeding the clinical deployment of mRNA vaccines is the energy depletion during mRNA translation, which also impedes the translation efficiency. The translation of mRNA into proteins is an energy-intensive process dependent on the sufficient supply of intracellular adenosine triphosphate (ATP), the primary energy currency within the cell.[20,21] Strikingly, the depletion of intracellular ATP levels triggered by mRNA translation enhances the efficiency of oxidative phosphorylation, an oxygen-consuming ATP synthesis pathway, leading to a swift decline in intracellular oxygen levels.[22,23] The reduction of the oxygen supply, along with the simultaneous exhaustion of cellular energy reserves, markedly constrains the mRNA translation, thus consequently compromising the therapeutic efficacy of mRNA vaccines.

The translation inefficiency of mRNA necessitates higher dosages of vaccines, escalating the risk and severity of potential adverse effects, thus attenuating their clinical viability. Remarkably, manganese oxide nanomaterial is able to catalyze the decomposition of hydrogen peroxide (H_2O_2) to generate

Received: September 3, 2024
Revised: November 6, 2024
Accepted: November 6, 2024
Published: November 18, 2024

https://doi.org/10.1021/jacs.4c12166
J. Am. Chem. Soc. 2024, 146, 32689−32700

Scheme 1. (a) Chemical Composition of Mn_3O_4 NPs and the Preparation of MnLNPs@mRNA Vaccine; (b) Schematic Illustration of MnLNPs@mRNA in Promoting DCs Maturation, Enhancing Antigen Presentation, Scavenging ROS, Activating cGAS-STING Pathway, and Boosting Antitumor Responses

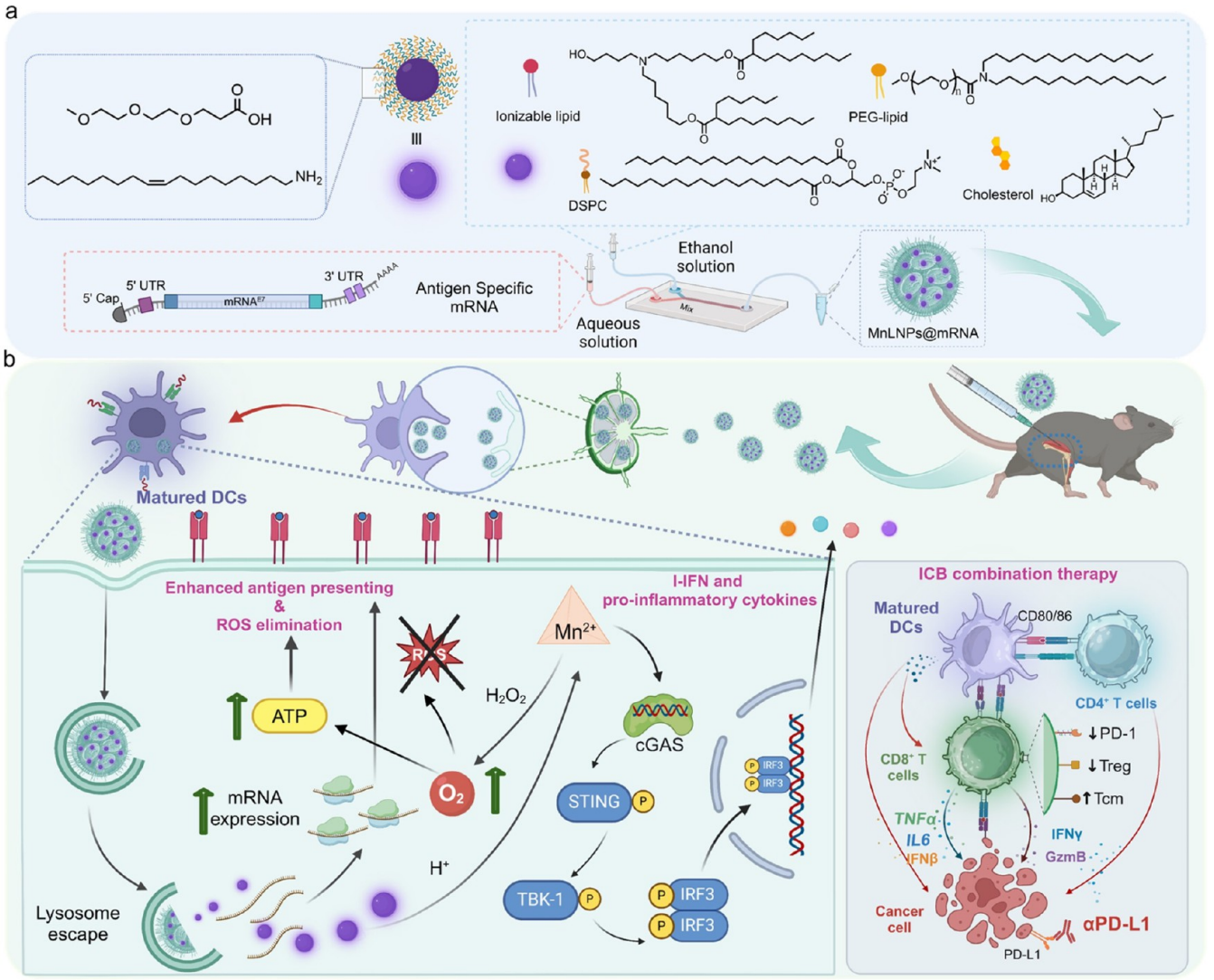

oxygen (O_2), which contributes to mitigating the transient hypoxia state induced by mRNA translation and elevating intracellular ATP levels, thereby boosting the mRNA translation efficiency.[21] Furthermore, Mn^{2+} ions have been identified as natural agonists for the cyclic guanosine monophosphate-adenosine monophosphate synthase (cGAS)-stimulator of interferon genes (STING) pathway,[24−30] which serves as a fundamental component of innate immune defenses, positioning manganese oxide nanomaterial as a potent enhancer of lipid nanoparticles (LNPs) for the fabrication of mRNA vaccines with higher therapeutic efficacy.

Herein, we propose a novel strategy that coassembles manganese tetroxide nanoparticles (Mn_3O_4 NPs) with classic LNPs to construct a hybrid mRNA delivery platform, MnLNPs, which allows to potentiate the therapeutic efficacy of mRNA vaccine by enhancing the translation efficiency of loaded mRNA (Scheme 1). Capitalizing on the potent ROS-scavenging and oxygen-generating capability, the transfection efficiency of dendritic cells (DCs) utilizing MnLNPs exhibits a notable augmentation when compared with four-component LNPs formulations. Intriguingly, the Mn^{2+} ions released from MnLNPs activate the cGAS-STING pathway, noticeably promoting DCs maturation and the secretion of type I interferons. Attributed to the enhanced antigen expression, the mRNA cancer vaccine (MnLNPs@mRNA^{E7}) using MnLNPs as a vehicle elicits potent antitumor immune responses and leads to enhanced infiltration of antigen-specific T lymphocytes into tumors. The superior antitumor performance is further amplified by combination with immune checkpoint blockade (ICB), which mitigates the immunosuppressive tumor microenvironment and reduces T cell exhaustion. MnLNPs exemplify the sophisticated strategy to overcome the obstacles faced by mRNA technology and herald the development of next-generation vaccines/therapeutics.

RESULTS AND DISCUSSION

Mn_3O_4 NPs were synthesized via a hydrothermal method using manganese acetate and oleylamine (Figure 1a). Unfortunately, the poor solubility of Mn_3O_4 NPs in ethanol limited their integration into LNPs (Figure S1). Therefore, we modified the surface of Mn_3O_4 NPs through ligand exchange by incorporating 3-[2-(2-methoxyethoxy)ethoxy]propanoic acid

https://doi.org/10.1021/jacs.4c12166
J. Am. Chem. Soc. 2024, 146, 32689−32700

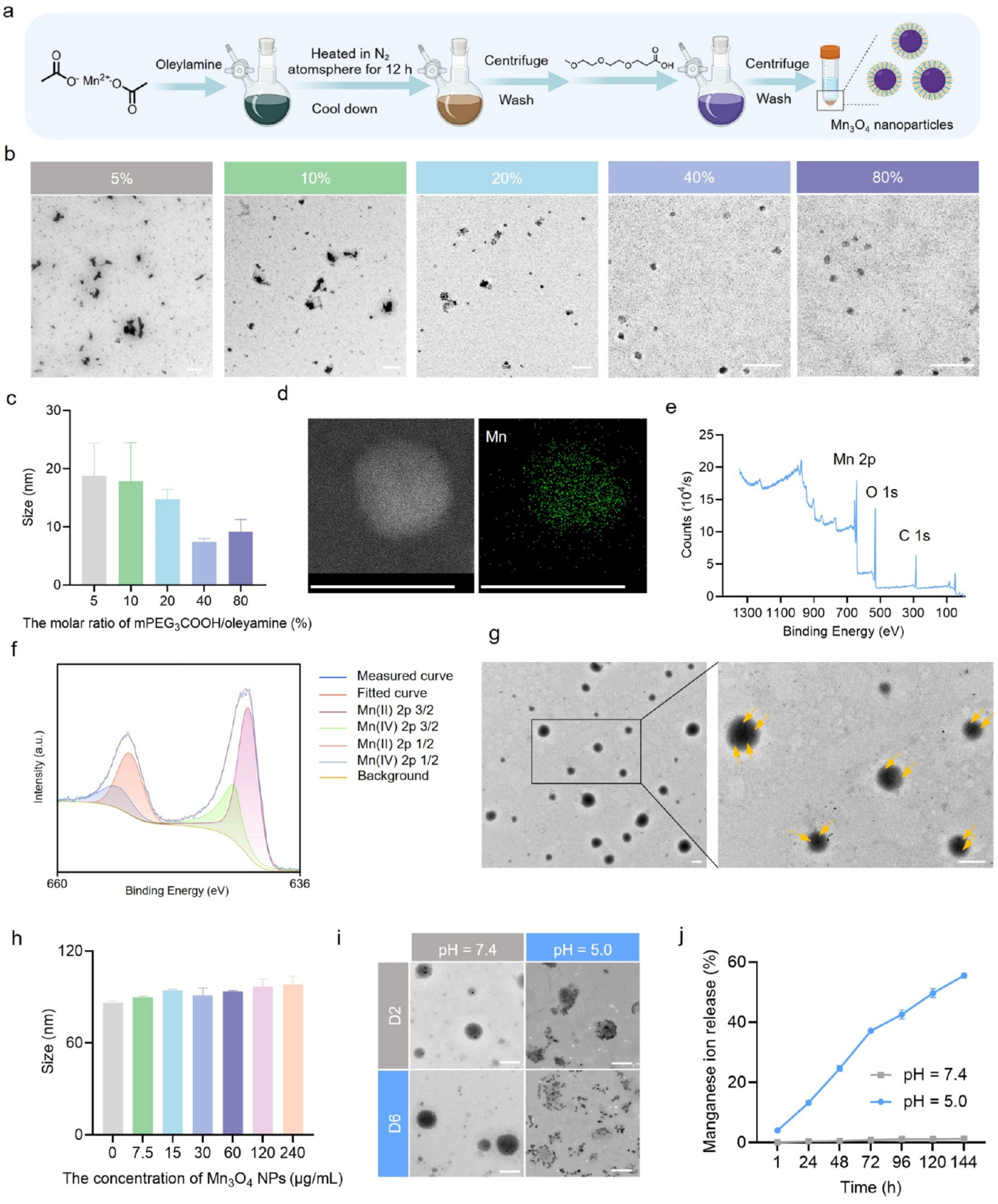

Figure 1. (a) Schematic illustration of the synthesis of Mn_3O_4 NPs and the subsequent surface ligand exchange. (b) TEM images (c) and particle size distribution of Mn_3O_4 NPs modified by $mPEG_3COOH$/oleylamine with different ratios. Scale bar: 50 nm. (d) Element mapping and (e, f) XPS spectra of Mn_3O_4 NPs. Scale bar: 10 nm. (g) TEM images of MnLNPs@mRNA. Yellow arrows indicate the Mn_3O_4 NPs. Scale bar: 100 nm. (h) Hydrodynamic size of MnLNPs@mRNA with different concentrations of Mn_3O_4 NPs. (i) TEM images of MnLNPs@mRNA cultured in aqueous solution at different pH values for 2 and 6 days. Scale bar: 100 nm. (j) The release profiles of manganese ion in PBS buffers (37 °C) at pH 7.4 and 5.0.

https://doi.org/10.1021/jacs.4c12166
J. Am. Chem. Soc. 2024, 146, 32689−32700

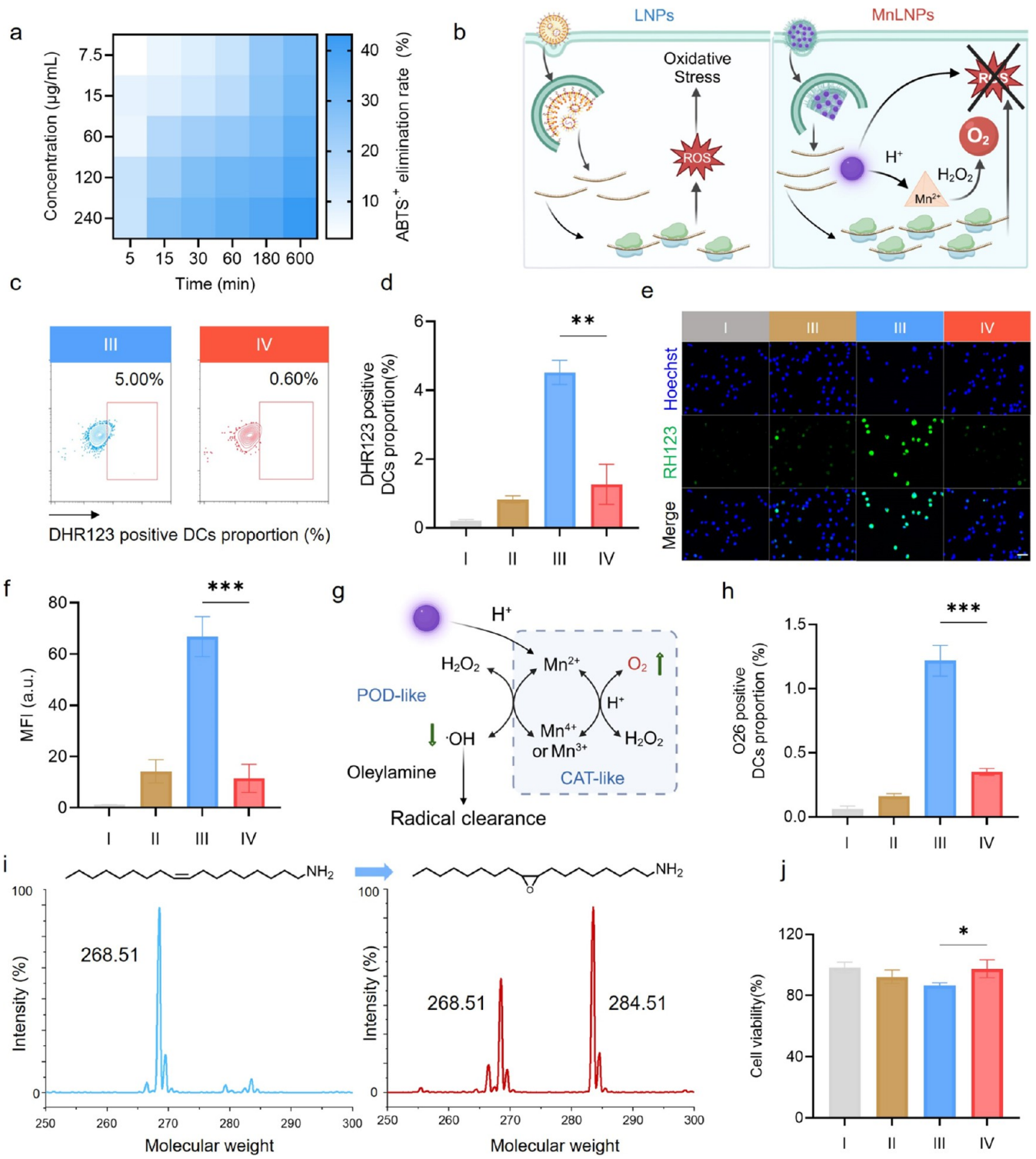

Figure 2. (a) Heatmap of the $ABTS^{\bullet+}$-scavenging ability of MnLNPs containing different concentrations of Mn_3O_4 NPs. (b) Schematic comparison of LNPs and MnLNPs in ROS scavenging. (c) Representative and (d) quantitative FCM analysis of RH 123-positive DCs after various treatments for 8 h using DHR 123 as a fluorescent probe of H_2O_2. (e) CLSM images and (f) MFI of DCs after various treatments for 8 h. Scale bar: 60 μm. (g) Schematic depiction of manganese ions undergoing Fenton-like reactions and decomposing H_2O_2. (h) Quantitative FCM results of the O26-positive DCs after various treatments for 8 h using the O26 as a $^{\bullet}OH$ probe. (i) LC-MS spectra of oleylamine before and after oxidation by $^{\bullet}OH$. (j) Cell viability of DCs after various treatments for 8 h. I: PBS, II: LNPs, III: LNPs@mRNA, IV: MnLNPs@mRNA, $^{*}p < 0.05$, $^{**}p < 0.01$, and $^{***}p < 0.001$.

($mPEG_3COOH$) with varying molar ratios, aiming to enhance the solubility of Mn_3O_4 NPs in ethanol (Figure 1a). Transmission electron microscopy (TEM) images and dynamic light scattering (DLS) measurements revealed serious aggregation between Mn_3O_4 NPs when the $mPEG_3COOH$/oleylamine ratio was 5 and 10% (Figures 1b,c, and S2−S5). Interestingly, the clusters of Mn_3O_4 NPs diminished with increased proportions of $mPEG_3COOH$, which is attributed to

https://doi.org/10.1021/jacs.4c12166
J. Am. Chem. Soc. 2024, 146, 32689−32700

the improved dispersity of NPs in ethanol. By increasing the $mPEG_3COOH$/oleylamine ratio to 40%, uniform NPs were obtained with an average diameter of 7.11 nm, which facilitated the successful integration into LNPs through a coassembly strategy driven by the hydrophobic interactions between the alkyl chains. However, the excessive modification of Mn_3O_4 NPs by $mPEG_3COOH$ resulted in a shift from amphiphilicity to hydrophilicity, which impeded the coassembly of Mn_3O_4 NPs and LNPs (Figure S6). As a consequence, the molar ratio of $mPEG_3COOH$ and oleylamine was optimized to 40% for the assembly. The Mn and O elements were confirmed through elemental mapping images of Mn_3O_4 NPs (Figure 1d). Additionally, X-ray photoelectron spectroscopy (XPS) analysis of Mn_3O_4 NPs revealed three primary peaks corresponding to Mn 2p (641.51 eV), O 1s (530.02 eV), and C 1s (284.80 eV). Further analysis of the spectra of Mn 2p indicated that Mn (IV) and Mn (II) dominated the materials in a ratio of 1:2 (Figure 1e,f). As depicted in Figure S7, the X-ray diffraction patterns of the acquired Mn_3O_4 NPs corresponded to the peaks of the standard tetragonal Mn_3O_4 reflection patterns (JCPDS #24−0734), demonstrating the successful preparation of Mn_3O_4 NPs.

MnLNPs loaded with mRNA (MnLNPs@mRNA) were formulated by mixing an aqueous mRNA solution with an ethanol solution containing Mn_3O_4 NPs and lipid mixture using a microfluidic chip. The lipid mixture was composed of ionizable lipid, cholesterol, PEG-lipid, and DSPC in a molar ratio of 46.4:42:1.6:10 (Scheme 1a). Given the critical impact of Mn_3O_4 NPs concentrations on MnLNPs performance, a series of MnLNPs@mRNA with increasing concentrations of Mn_3O_4 NPs were formulated and subjected to screening *in vitro*. DLS results depicted a consistent diameter of approximately 90 nm with low polydispersity indexes (<0.20) for all MnLNPs@mRNA, indicating the minimal impact of Mn_3O_4 NPs incorporation on the self-assemblies (Figures 1h and S8−S15). Subsequently, the optimal concentration of Mn_3O_4 NPs was determined at 60 μg/mL, which yielded the highest translation efficiency and exhibited negligible toxicity to mammalian cells (Figures S16 and S17).

Upon formulation optimization, the physicochemical characteristics of MnLNPs@mRNA were further elucidated. As illustrated in Figure 1g, the TEM images distinctly depicted the successful incorporation of Mn_3O_4 NPs within the MnLNPs@mRNA nanospheres. Notably, the average diameter was decreased from 187.5 ± 4.3 to 92.9 ± 3.8 nm after mRNA encapsulation (Figures 1h and S18), ascribed to the electrostatic interactions between the negatively charged mRNA and the ionizable lipid. This size decrease was further substantiated by TEM images before and after mRNA loading (Figure S19). Furthermore, MnLNPs@mRNA maintained stability in PBS at pH 7.4 over 6 days yet rapidly disintegrated at pH 5.0, dissociating the spherical structure (Figure 1i). The manganese ion release profile from MnLNPs@mRNA at 37 °C at different pH values was also measured by inductively coupled plasma mass spectroscopy. Within 96 h, the cumulative release rate of manganese ion at pH 5.0 reached 42.0%, in stark contrast to the 1.10% observed at pH 7.4, indicating the accelerated degradation of Mn_3O_4 NPs into manganese ion in an acidic environment.

The antioxidant capacity of MnLNPs was assessed by utilizing 2,2′-azino-bis(3-ethylbenzthiazoline-6-sulfonic acid) (ABTS) as a chromogenic agent. ABTS can be oxidized into green $ABTS^{\bullet+}$, and antioxidants can reverse this process. As summarized in Figures 2a and S20, at a concentration of 60 μg/mL Mn_3O_4 NPs, MnLNPs scavenged 30.1% of $ABTS^{\bullet+}$ within 180 min, implying their antioxidant potential, which is beneficial to augment mRNA translation efficiency. As shown in Figure 2b, it was noteworthy that the treatment of LNPs@mRNA significantly upregulated intracellular ROS, causing oxidative stress, which impedes mRNA translation. In sharp contrast, the oxidative stress was effectively alleviated by using MnLNPs as the vehicle of the mRNA vaccine due to the outstanding capability of Mn_3O_4 NPs in scavenging ROS. Intracellular levels of H_2O_2 were evaluated by using dihydrorhodamine 123 (DHR 123) as a fluorescent probe through flow cytometry (FCM) and confocal laser scanning microscopy (CLSM). The nonfluorescent DHR 123 can become brightly emissive after being oxidized into RH 123. As depicted in Figure 2c,d, cells treated with LNPs@mRNA demonstrated accumulated intracellular H_2O_2, indicating possible oxidative stress during mRNA translation using LNPs. Notably, MnLNPs@mRNA significantly reduced the level of intracellular H_2O_2, as demonstrated by the reduction in the percentage of RH 123-positive cells from 5.01 to 0.60%. In line with the FCM results, LNPs@mRNA treatment led to much brighter green fluorescence compared with PBS treatment, signifying the overproduction of intracellular H_2O_2 induced using LNPs as the mRNA delivery system. On the contrary, treatment with MnLNPs@mRNA was observed to ameliorate oxidative stress through scavenging excessive H_2O_2 generated during mRNA translation. Cells treated with MnLNPs@mRNA exhibited a markedly diminished fluorescence signal, with an intensity that was only 17.2% of that observed in cells treated with LNPs@mRNA, underscoring the formidable ROS-scavenging capability of MnLNPs (Figure 2e,2f).

Mn^{2+} undergoes a Fenton-like reaction in the presence of H_2O_2, inducing the generation of hydroxyl radicals ($^{\bullet}OH$), which further exacerbates the oxidative stress during mRNA translation (Figure 2g).[12,15,30] The intracellular $^{\bullet}OH$ levels were monitored by using O26 as the fluorescent indicator. Strikingly, strong green fluorescence was observed inside cells treated with LNPs@mRNA, however, negligible signal was detected in the MnLNPs@mRNA-treated group, highlighting the $^{\bullet}OH$-scavenging capability of MnLNPs (Figure S21). The results were further confirmed through quantitative FCM results (Figure 2h). We attributed the antioxidative ability of MnLNPs to the unsaturated bonds of oleylamine on the surface of Mn_3O_4 NPs, which were able to react with various oxidants. As demonstrated in Figure 2i, liquid chromatography−mass spectrometry (LC-MS) was used to analyze the products after oxidation by $^{\bullet}OH$, which demonstrated that the unsaturated bond of oleylamine was mainly oxidized into epoxide. Except from the capability to mitigate oxidative stress, MnLNPs recovered cell viability to that of the PBS-treated group (Figure 2j), emphasizing their promising performance in mRNA translation.

We proceeded to analyze the impact of MnLNPs on mRNA translation in DCs using enhanced green fluorescent protein (EGFP)-encoding mRNA ($mRNA^{EGFP}$). To simulate the hypoxia and energy-depleted environment caused by mRNA translation, DC 2.4 cells were incubated in a hypoxic chamber where the oxygen concentration was less than 1% and treated with MnLNPs@$mRNA^{EGFP}$ containing different concentrations of Mn_3O_4 NPs for 12 h. Subsequently, the translation of $mRNA^{EGFP}$ was evaluated through FCM and CLSM. As

https://doi.org/10.1021/jacs.4c12166
J. Am. Chem. Soc. 2024, 146, 32689−32700

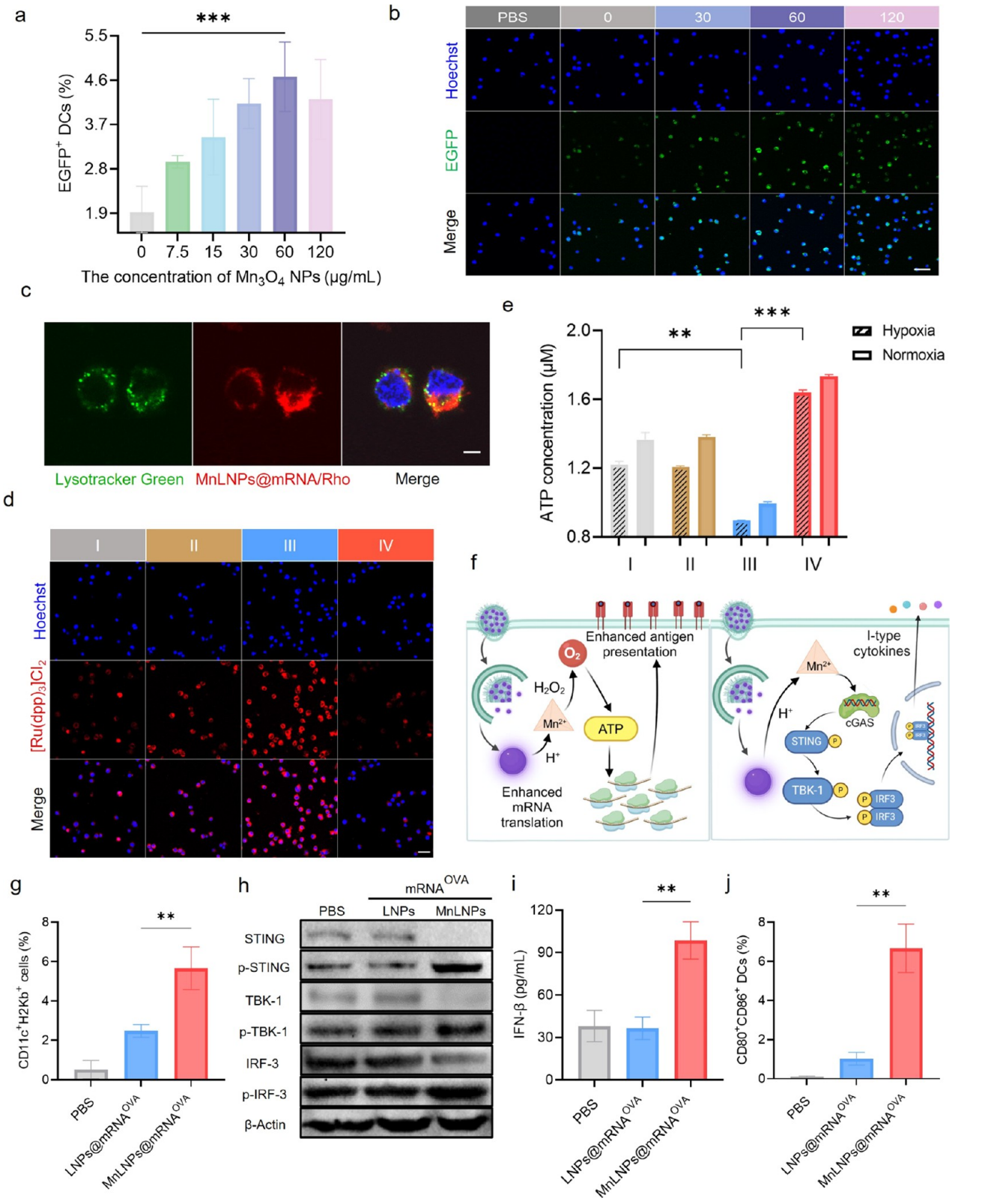

Figure 3. (a) Quantitative FCM results and (b) CLSM images of EGFP$^+$ DCs treated with MnLNPs@mRNA^{EGFP} at different concentrations of Mn_3O_4 NPs in a hypoxic environment. Scale bar: 40 μm. (c) CLSM images of DCs treated with Rhodamine 6G-labeled MnLNPs@mRNA. Scale bar: 5 μm. (d) CLSM images of DCs treated with different formulations for 12 h using $[Ru(dpp)_3]Cl_2$ as a hypoxia probe. Scale bar: 40 μm. (e) Quantitative analysis of intracellular ATP after various treatments for 12 h. (f) Schematic illustration of the enhanced mRNA translation efficiency and cGAS-STING pathway activation by MnLNPs@mRNA. (g) Quantitative FCM results of CD11c$^+$H2Kb$^+$ DCs after different treatments. (h) Immunoblot analysis of STING, TBK-1, and IRF-3 in DCs after different treatments. (i) IFN-β levels in the supernatant of DCs after different treatments. (j) Quantitative analysis of CD80$^+$CD86$^+$ DCs after various treatments. I: PBS, II: LNPs, III: LNPs@mRNA, IV: MnLNPs@mRNA. *p < 0.05, **p < 0.01, and ***p < 0.001.

https://doi.org/10.1021/jacs.4c12166
J. Am. Chem. Soc. 2024, 146, 32689−32700

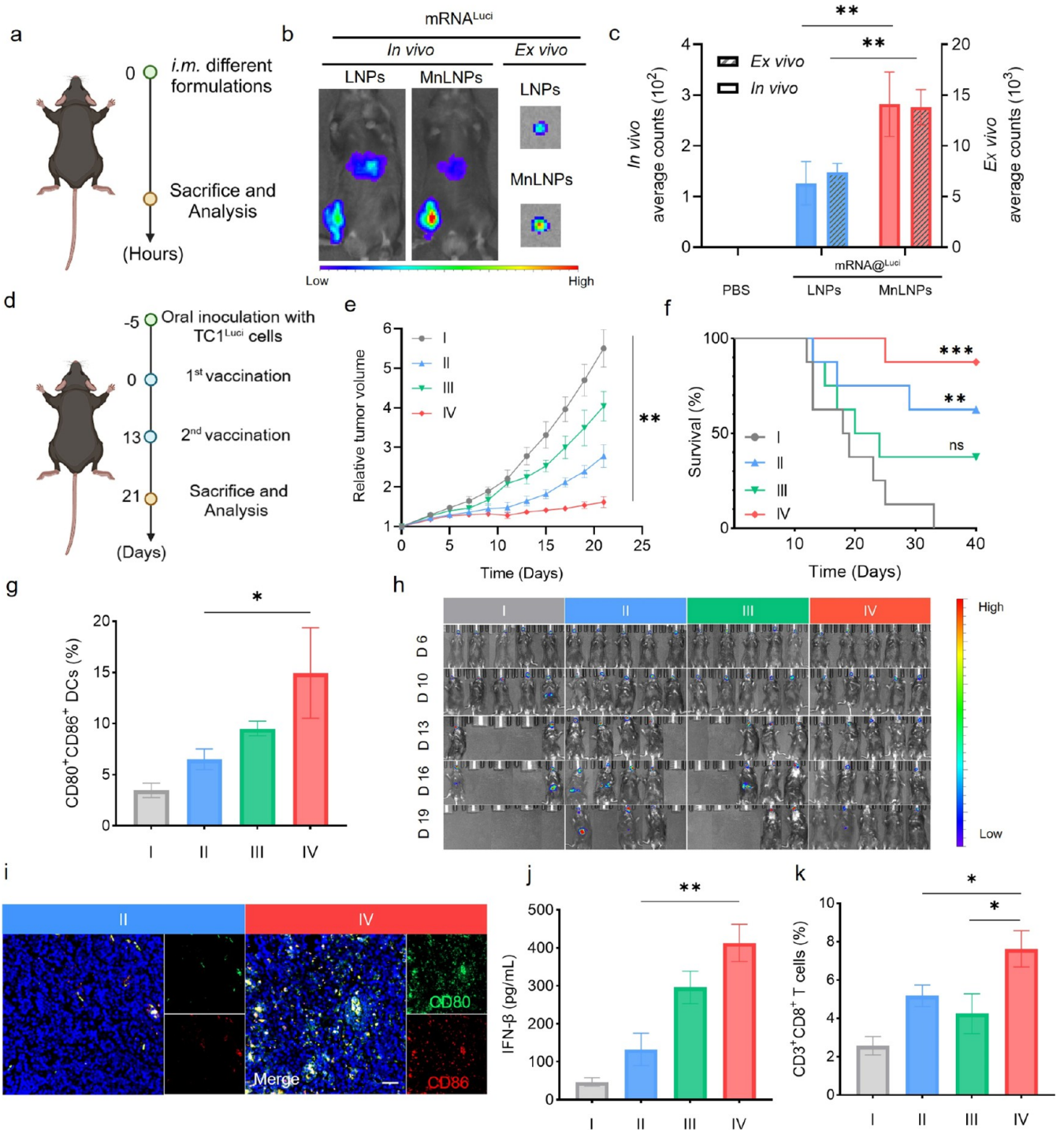

Figure 4. (a) Analysis of the mRNA translation efficiency *in vivo*. (b) *In vivo* and *ex vivo* imaging of mice after treatment with LNPs@mRNA^{Luci} and MnLNPs@mRNA^{Luci}. (c) Statistical results of bioluminescence intensity from the mice after various treatments. (d) Therapeutic schedule of mice bearing TC-1^{Luci} tumors. (e) Relative tumor volume profiles and (f) survival rates of the mice after different treatments. (g) Percentage of $CD80^+CD86^+$ DCs in lymph nodes. (h) Representative bioluminescence images of tumor-bearing mice from day 6 to day 19. (i) Immunofluorescence images of $CD80^+$ and $CD86^+$ cells in lymph nodes from the mice in groups II and IV. Scale bar: 100 μm. (j) IFN-β levels in serum and (k) proportions of $CD3^+CD8^+$ T cells in tumors after various treatments. I: PBS, II: LNPs@mRNA^{E7}, III: MnLNPs, IV: MnLNPs@mRNA^{E7}. $^*p < 0.05$, $^{**}p < 0.01$, and $^{***}p < 0.001$.

demonstrated in Figure 3a, the mRNA translation efficiency decreased by 1 order of magnitude in the hypoxic environment compared with normoxia (Figure S16), providing convincing evidence for the reduced mRNA translation efficiency caused by oxygen deficiency. Notably, MnLNPs@mRNA^{EGFP} presented an overwhelming superiority of translation efficiency over that of LNPs@mRNA^{EGFP} at the Mn_3O_4 NPs concentration of 60 μg/mL, reaching 2.5 times that of the LNPs@mRNA^{EGFP} treatment (Figures 3a and S22). Consistently, a higher proportion of DCs expressing EGFP from the MnLNPs@mRNA^{EGFP}-treated group was observed in the

https://doi.org/10.1021/jacs.4c12166
J. Am. Chem. Soc. 2024, 146, 32689−32700

CLSM images, further confirming the promoted translation efficiency of MnLNPs compared with LNPs (Figure 3b).

The translation of mRNA involves the processes of cellular uptake, endo/lysosomal escape, and translation by ribosomes, of which each step influences the final translation efficiency. Subsequent evaluation encompassed the cellular uptake process and endo/lysosomal escape capability of MnLNPs@mRNA to uncover mechanisms under the exceptional DCs transfection ability of MnLNPs. DCs were incubated with Rhodamine-labeled MnLNPs@mRNA for 8 h before CLSM analysis. As depicted in Figure S23, a significant red signal from Rhodamine indicated that DCs internalized a substantial amount of MnLNPs@mRNA, forming the basis for the high transfection efficiency of MnLNPs@mRNA. Furthermore, the distinct separation between the red signal from Rhodamine-labeled MnLNPs@mRNA and the green signal from Lysotracker Green suggested the successful endo/lysosomal escape of MnLNPs@mRNA and their translocation to the cytoplasm (Figure 3c).

Based on the preceding results, we proposed that the mRNA translation efficiency was substantially compromised by the diminished intracellular oxygen and energy availability. Fortunately, MnLNPs containing Mn_3O_4 NPs were capable of decomposing H_2O_2 to produce oxygen (Figures 2g and S25), suggesting the potential of MnLNPs to alleviate the hypoxic state engendered by mRNA translation. As shown in Figure S24, MnLNPs prompted the generation of 6 mg/L of dissolved oxygen within 30 min at pH 6.5, which was 10-fold that of LNPs. The exceptional oxygen-generating capacity of MnLNPs contributed to the enhanced translation efficiency of MnLNPs@mRNA. Furthermore, tris(4,7-diphenyl-1,10-phenanthroline)ruthenium(II) dichloride ($[Ru(dpp)_3]Cl_2$) was chosen as a hypoxic fluorescent probe to detect intracellular hypoxia, with its red fluorescence being quenched by oxygen. Astonishingly, intense red fluorescence was detected in the cells treated with LNPs@mRNA, suggesting that the mRNA vaccine based on LNPs rapidly depleted intracellular oxygen during mRNA translation, leading to an instantaneously hypoxic environment, which dramatically impeded mRNA translation. In sharp contrast, MnLNPs markedly ameliorated intracellular hypoxia state, as evidenced by the negligible red fluorescence detected in DCs treated with MnLNPs@mRNA, highlighting the potential of MnLNPs in boosting mRNA translation by elevating intracellular oxygen levels (Figure 3d).

Increased intracellular oxygen was able to accelerate oxidative phosphorylation, thereby enhancing the generation of adenosine triphosphate (ATP), the cellular energy currency essential for translating mRNA into protein.[22,23] Notably, MnLNPs@mRNA triggered a 26.1% increase of intracellular ATP level compared with that of the PBS group, outperforming LNPs in alleviating cellular energy exhaustion and facilitating mRNA translation (Figure 3e). As summarized in Figure 3f, upon successful uptake and endo/lysosomal escape, MnLNPs@mRNA can decompose the H_2O_2 generated during mRNA translation to produce oxygen, thereby elevating intracellular ATP levels and contributing to the enhanced expression of loaded mRNA. Furthermore, the antigen presentation capacity of MnLNPs-treated DCs was evaluated. DCs were treated with various formulations encapsulating ovalbumin-encoding mRNA ($mRNA^{OVA}$), and the antigen presentation efficiency was analyzed by FCM. Benefiting from the exceptional mRNA transfection efficiency, MnLNPs@$mRNA^{OVA}$ achieved 5.71% $CD11c^+H2Kb^+$ DCs, surpassing the 2.52% of LNPs@$mRNA^{OVA}$ treatment (Figure 3g), which demonstrated the excellent antigen presentation capability and antitumor potency of mRNA vaccine using MnLNPs as a vehicle.

Intriguingly, Mn^{2+} ions could act as agonists for the cGAS-STING pathway that is known to facilitate DCs maturation and cytokines secretion, such as type I interferons and interleukins, thus activating innate and adaptive immunity.[25−27,29] Notably, MnLNPs have been observed to enhance the phosphorylation levels of STING, TBK-1, and IRF-3 in comparison to LNPs, proving that MnLNPs were able to effectively promote the activation of the cGAS-STING pathway (Figure 3h). Additionally, cytokine secretion stimulated by various formulations was measured using enzyme-linked immunosorbent assay (ELISA). The elevated levels of IFN-β and IL-6 in cells treated with MnLNPs@$mRNA^{OVA}$ provided compelling evidence for their capability to activate the cGAS-STING pathway (Figures 3i and S26). As depicted in Figure 3j, the upregulated expression of costimulatory molecules in DCs was observed in the treatment of MnLNPs@$mRNA^{OVA}$. The administration of MnLNPs@$mRNA^{OVA}$ promoted the proportion of $CD80^+CD86^+$ DCs to 6.72%, signifying robust DCs maturation driven by MnLNPs-mediated activation of the STING pathway. The improved translation efficiency of tumor antigen mRNA and the activation of the STING pathway suggested that MnLNPs have considerable potential in enhancing the therapeutic efficacy of mRNA tumor vaccine.

To investigate the biodistribution and *in vivo* translation efficiency of MnLNPs@mRNA, DiR and firefly luciferase-encoding mRNA ($mRNA^{Luci}$) were respectively encapsulated by MnLNPs, which were intramuscularly (*i.m.*) injected in the thigh of mice (Figure 4a). Fluorescence imaging demonstrated that no obvious accumulation of these two formulations (LNPs@DiR and MnLNPs@DiR) was observed in major organs, such as heart, spleen, lung, and kidney (Figure S27). Interestingly, the fluorescence intensity of the two formulations was comparable in the draining lymph nodes (dLNs), with relative radiant efficiency reaching 20% at 12 h, while the bioluminescence signal was substantially different. Both *in vivo* and *ex vivo* imaging indicated that MnLNPs@$mRNA^{Luci}$ administration demonstrated stronger bioluminescence than LNPs@$mRNA^{Luci}$ in both the injected muscle and dLNs, providing persuasive proof of enhanced mRNA translation facilitated by MnLNPs (Figure 4b). Consistently, quantification analysis proved that the mRNA translation efficiency was markedly improved by MnLNPs as its bioluminescence intensity in lymph nodes was 2-fold that of LNPs@mRNA (Figure 4c). Additionally, the *in vivo* antigen presentation of MnLNPs@$mRNA^{OVA}$ was further assessed through FCM after *i.m.* injection with different formulations encapsulating $mRNA^{OVA}$. Ascribing to the enhanced translation efficiency, MnLNPs@$mRNA^{OVA}$ induced a higher proportion of $CD11c^+H2kb^+$ DCs in draining lymph nodes, amounting to 7.87%, which was 1.5-fold that of LNPs@$mRNA^{OVA}$ (Figure S28), underscoring the exceptional ability of MnLNPs to enhance antigen presentation. Furthermore, the elevated proportion of antigen-specific $CD8^+$T cells from 5.19% to 12.6% in the peripheral blood of MnLNPs@$mRNA^{OVA}$-treated mice not only confirmed the upregulated antigen presentation by MnLNPs but also demonstrated the potent capability of the

https://doi.org/10.1021/jacs.4c12166
J. Am. Chem. Soc. 2024, 146, 32689−32700

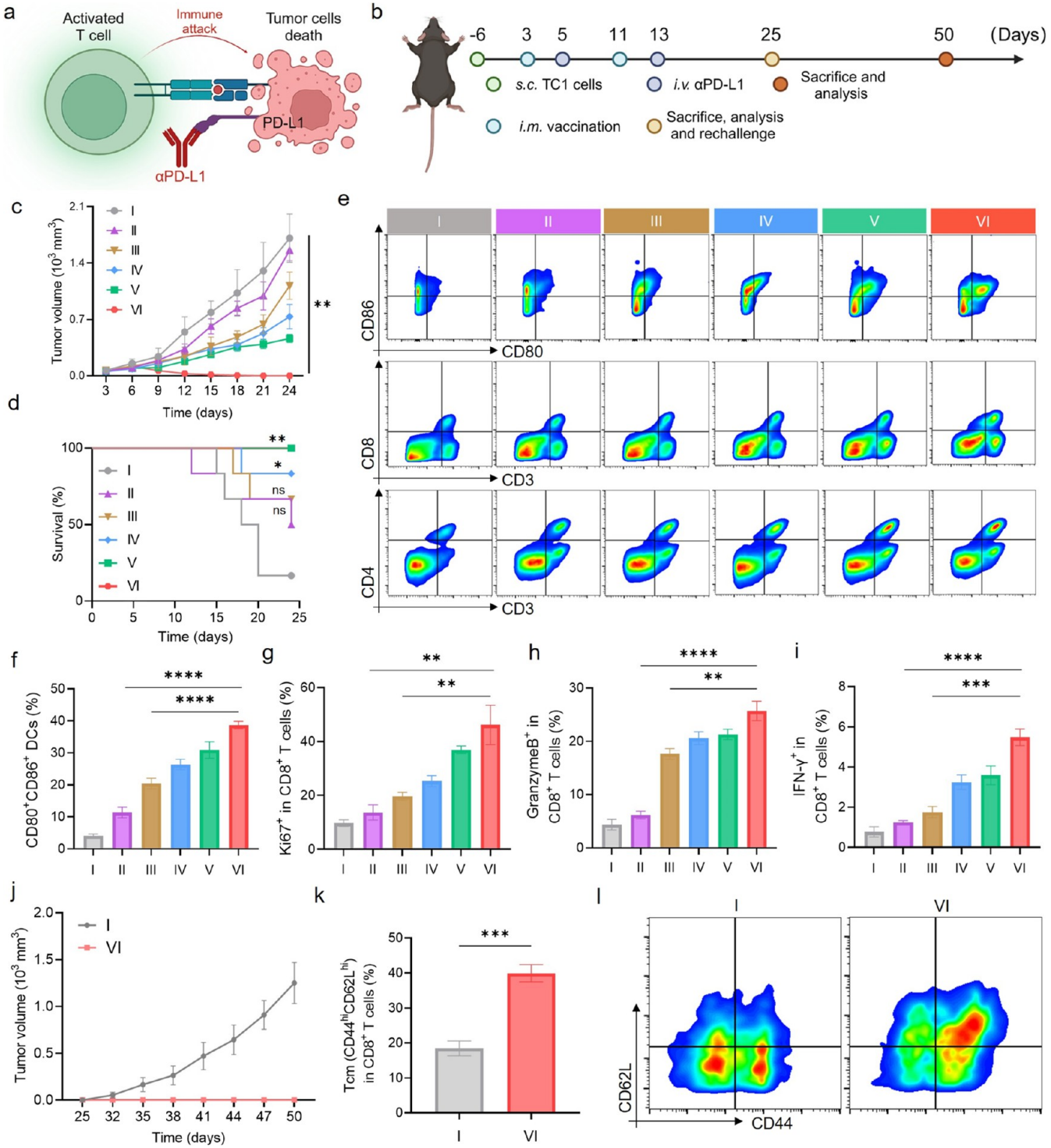

Figure 5. (a) Schematic illustration of immunotherapy. (b) Therapeutic schedule of mice bearing TC-1 tumor. (c) Tumor volume profiles and (d) survival rates of mice after different treatments. (e) Representative FCM results of $CD80^+CD86^+$ DCs in lymph nodes, intratumoral $CD3^+CD4^+$ T cells, and intratumoral $CD3^+CD8^+$T cells from the mice after different treatments. (f) Statistical results of $CD80^+CD86^+$ DCs in lymph nodes from mice after different treatments. Analysis of $CD8^+$ T cell phenotypes within the tumors, including (g) $Ki67^+$ in $CD8^+$ T cells, (h) granzyme B $(GrzmB)^+$ in $CD8^+$ T cells, and (i) $IFN\gamma^+$ in $CD8^+$ T cells. (j) Tumor growth curves following rechallenge with subcutaneous TC1 in PBS- and $MnLNPs@mRNA^{E7}$ + αPD-L1-treated mice. (k) Quantitative and (l) representative FCM results of memory T cells in the spleen after rechallenge. I: PBS, II: αPD-L1, III: $LNPs@mRNA^{E7}$, IV: $LNPs@mRNA^{E7}$ + αPD-L1, V: $MnLNPs@mRNA^{E7}$, VI: $MnLNPs@mRNA^{E7}$ + αPD-L1. $^*p < 0.05$, $^{**}p < 0.01$, $^{***}p < 0.001$, and $^{****}p < 0.001$.

MnLNPs-based mRNA vaccine in activating antitumor immunity (Figure S29).

Encouraged by the excellent translation efficiency and antigen presentation ability of MnLNPs@mRNA *in vivo*, the antitumor efficacy of the MnLNP-based mRNA vaccine was assessed on the orthotopic oral cancer model. Mice were immunized with PBS, $LNPs@mRNA^{E7}$ (encapsulating HPV-specific antigen-encoding $mRNA^{E7}$), and MnLNPs and

https://doi.org/10.1021/jacs.4c12166
J. Am. Chem. Soc. 2024, 146, 32689−32700

MnLNPs@mRNA^{E7}, respectively (Figure 4d). The antitumor efficacy of these formulations was evaluated by tracing the tumor growth profile (Figure 4e) and calculating the tumor inhibitory rates (TIR) according to the equation: TIR = [{1 − (mean tumor volume of treated groups)/(mean tumor volume of PBS group)} × 100(%)]. Compared with the PBS-treated group, MnLNPs alone induced only marginal tumor suppression, which was possibly attributed to the activation of innate immunity. Regrettably, LNPs@mRNA^{E7} resulted in unsatisfactory tumor inhibition with a TIR of 49.5%, mainly because of inefficient antigen expression in activating T cell immune responses. Encouragingly, the mice immunized with MnLNPs@mRNA^{E7} exhibited outstanding tumor suppression, with a TIR of 70.7%. The outperforming efficacy of MnLNPs@mRNA^{E7} was further elucidated through *in vivo* imaging (Figures 4h and S31). Luminescence imaging confirmed that the mice treated with MnLNPs@mRNA^{E7} exhibited the most superb antitumor efficacy, with 3 mice achieving complete tumor regression. Strikingly, the mice treated with LNPs@mRNA^{E7} displayed notable hepatic metastasis, as evidenced by the pronounced hepatic bioluminescence intensity, which was not observed in the MnLNPs@mRNA^{E7} group, further demonstrating the exceptional efficacy of the MnLNPs-based mRNA vaccine. Additionally, benefiting from the boosted antitumor immunity, mice vaccinated with MnLNPs@mRNA^{E7} exhibited prolonged median survival and reduced mortality rates to 12.5% during treatment (Figures 4f and Figure S35).

As mentioned before, MnLNPs were capable of activating the cGAS-STING pathway, thereby promoting the stable maturation of DCs. The expression level of CD86 and CD80 was assessed through FCM to uncover the maturation of DCs in the vaccinated mice. As illustrated in Figure 4g, the matured DCs in the mice immunized with MnLNPs@mRNA^{E7} reached 14.9%, surpassing that of LNPs@mRNA^{E7}-treated group. Corroborating the FCM data, immunofluorescence staining of lymph nodes from MnLNPs@mRNA^{E7}-treated mice revealed an increased expression of CD80 and CD86 biomarkers on DCs, in sharp comparison to the LNPs@mRNA^{E7} group (Figures 4i and S32). Furthermore, *in vivo* activation of the STING pathway mediated by MnLNPs was substantiated by the elevated levels of IL-6 and IFN-β in serum, which were indicative of the augmented immune activation conferred by the MnLNPs@mRNA^{E7} tumor vaccine (Figures 4j and S33).

T cell activation is a crucial step of the antitumor immune response, which ensures the efficacy of mRNA tumor vaccine. Beyond matured DCs and enhanced cytokine levels, T cells were substantially activated for the mice vaccinated with MnLNPs@mRNA^{E7}, as indicated by the augmented population of tumor-infiltrating lymphocytes (TILs). Specifically, the administration of MnLNPs@mRNA^{E7} markedly increased the proportion of intratumoral CD3$^+$CD8$^+$ T cells from 5.18 to 7.63%, much higher than that of LNPs@mRNA^{E7} treatment (Figures 4k and S34). Likewise, the prevalence of CD3$^+$CD4$^+$ T cells in tumors from MnLNPs@mRNA^{E7}-vaccinated mice reached 10.1%, exceeding that of LNPs@mRNA^{E7} vaccination (7.30%). The enhancement of TILs highlighted the superior capacity of MnLNPs@mRNA^{E7} to bolster adaptive immunity compared with LNPs@mRNA^{E7}, thereby signifying the potency of the mRNA vaccine using MnLNPs as the delivery vehicle.

It is frustrating that the efficacy of tumor immunotherapy was typically undermined by the immune escape of tumor cells.[31,32] These cells express programmed cell death ligand 1 (PD-L1) on their surface, which serves to inhibit the proliferation and functionality of T cells, consequently promoting the initiation and metastasis of tumors. Moreover, a notable upsurge in PD-L1 expression has been documented in HPV-positive tumors, highlighting the prospective therapeutic value of anti-PD-L1 antibodies (αPD-L1) in the management of HPV-associated malignancies.[33,34] ICB therapy, which employs αPD-L1 to block the PD-1/PD-L1 axis, rejuvenates exhausted T cells and restores antitumor immune responses (Figure 5a). To augment the antitumor potency of MnLNPs@mRNA^{E7}, αPD-L1 was *i.v.* injected on days 8 and 16 to counteract the immunosuppression (Figure 5b). Figures 5c and S37−S42 demonstrate that monotherapy using either αPD-L1 or LNPs@mRNA^{E7} led to marginal tumor suppression with a TIR of 8.87 and 34.5%, respectively. This underscored the limitations of ICB and LNPs-based mRNA vaccines in halting tumor progression. While the combination of LNPs@mRNA^{E7} and αPD-L1 improved the antitumor effects, the results were suboptimal due to inadequate antigen presentation and T cell activation. Excitingly, MnLNPs@mRNA^{E7} + αPD-L1 demonstrated superior antitumor efficacy, as evidenced by the complete elimination of tumors in three vaccinated mice. In addition, combination therapy elicited a higher ratio of apoptotic tumor cells (45.1%) compared with that of the LNPs@mRNA^{E7} group (22.7%), underscoring its exceptional efficacy in tumor suppression (Figure S44). The Kaplan−Meier survival plots further revealed that mice administrated with MnLNPs@mRNA^{E7} + αPD-L1 exhibited the longest survival over 80 days without a single death, primarily due to the potent tumor inhibition (Figures 5d and S43).

Specifically, the combination therapy markedly elevated cytokine levels (IL-6 and IFN-β) and the frequency of CD86$^+$CD80$^+$ DCs in lymph nodes, signifying the robust adaptive immune responses stimulated by STING activation (Figures 5e,f, and S45−S46). Additionally, a significant rise in the population of tumor-infiltrating T lymphocytes was monitored in the mice treated with MnLNPs@mRNA^{E7} + αPD-L1, the proportion of CD3$^+$CD4$^+$ and CD3$^+$CD8$^+$ T cells reached 20.5 and 11.5%, respectively (Figures 5e and S47 and S48). The synergy of combination therapy elicited the highest intratumoral cytokine concentrations, including IL-12, IFN-γ, and TNF-α, thereby potentiating antitumor immune responses (Figure S45).

In line with the increased levels of TILs, subsequent analysis of the phenotype of CD8$^+$ T cells isolated from tumors revealed that the proportion of Ki67$^+$ cytotoxic T lymphocytes (CTLs) in tumors from mice treated with MnLNPs@mRNA^{E7} + αPD-L1 rose to 46.1%, exceeding those treated with αPD-L1 or LNPs@mRNA^{E7} (Figure 5g). The combination of MnLNPs@mRNA^{E7} and αPD-L1 not only augmented the percentage of tumor-infiltrating T cells that produce the pro-inflammatory cytokines, like IFN-γ and granzyme B (Figure 5h,5i) but also reduced the proportion of T cells coexpressing inhibitory receptors PD-1, indicative of enhanced effector T cell functionality (Figure S49). Furthermore, the combination therapy successfully remodeled the immunosuppressive tumor microenvironment (TME) with a decreased percentage of Foxp3$^+$ in CD4$^+$ T cells (regulatory T cells, Treg) in the mice treated with MnLNPs@mRNA^{E7} + αPD-L1, leading to

https://doi.org/10.1021/jacs.4c12166
J. Am. Chem. Soc. 2024, 146, 32689−32700

substantial tumor regression (Figure S50). The enduring immunological impact of MnLNPs@mRNA^{E7} + αPD-L1 was further investigated through a tumor rechallenge study (Figure 5a). Remarkably, rechallenging tumor-free mice from combination therapy with homotypic cells exhibited complete tumor rejection, suggesting the establishment of long-term immunological antitumor memory (Figure 5j). Specifically, MnLNPs@mRNA^{E7} + αPD-L1 treatment induced 40.4% of central memory T cells (Tcm), a substantial increase compared with the PBS group (Figure 5k,5l), confirming the potential of MnLNPs-based mRNA vaccine as a powerful and sustained anticancer modality.

Furthermore, ensuring the safety of the mRNA vaccine is critical for their clinical application with minimal adverse effects. Systemic toxicity was assessed by monitoring body weight changes of mice throughout the treatment period, with no notable weight loss observed in mice treated with MnLNPs@mRNA^{E7} or the combination therapy (Figures S30 and S36). Histopathological analysis with hematoxylin and eosin (H&E) staining of major organs revealed no evidence of tissue damage after treatment, affirming the biocompatibility and safety of the MnLNPs-based mRNA vaccine (Figure S51).

MnLNPs hold immense promise in the field of mRNA vaccines and therapeutics. Their outstanding ability to generate oxygen and scavenge ROS greatly promoted mRNA translation and antigen expression, which not only enhanced the efficacy of classic vaccines but also paved the way for developing new vaccines against a broader range of diseases. Besides, the activation of both innate and adaptive immune responses caused by MnLNPs led to strong and long-lasting immunity, offering a more comprehensive approach to disease prevention, especially for challenging infectious diseases like human immunodeficiency virus.

CONCLUSIONS

In summary, we proposed a potent strategy to augment the efficacy of mRNA vaccines through enhancing mRNA translation efficiency and activating the STING pathway. The strategy involved coassembling Mn_3O_4 NPs with classic LNPs, forming a hybrid mRNA delivery system, denoted as MnLNPs. The incorporation of Mn_3O_4 NPs not only eliminated the ROS and free radicals produced during mRNA translation but also elevated intracellular ATP levels by promoting O_2 generation, resulting in a substantial enhancement of mRNA transfection efficiency. Moreover, the released Mn^{2+} from MnLNPs activated the STING pathway to promote DCs maturation and the secretion of cytokines, which were favorable to eliciting both innate and adaptive immune responses. Leveraging the boosted antitumor immune responses, MnLNPs@mRNA^{E7} dramatically accelerated the infiltration of cytotoxic T cells into the tumor and remodeled the immunosuppressive TME, ultimately leading to substantial tumor suppression. Notably, the therapeutic efficacy of MnLNPs@mRNA^{E7} was further augmented by combining with ICB, intensifying the lethality of T cells, and achieving a sustained antitumor effect. With excellent capacity to generate aqueous O_2 while activating the STING pathway, MnLNPs outperform LNPs in enhancing mRNA translation efficiency and stimulating the antitumor immune response of mRNA vaccines, which position them as a highly promising strategy in the fabrication of mRNA vaccines for cancer therapy.

ASSOCIATED CONTENT

Supporting Information

The Supporting Information is available free of charge at https://pubs.acs.org/doi/10.1021/jacs.4c12166.

Materials; methods; chemical characterizations; Western blot; flow cytometry; CLSM images (PDF)

AUTHOR INFORMATION

Corresponding Author

Guocan Yu − *Ministry of Education Key Laboratory of Bioorganic Phosphorus Chemistry & Chemical Biology, Department of Chemistry, Tsinghua University, Beijing 100084, P. R. China;* orcid.org/0000-0003-1157-4184; Email: guocanyu@mail.tsinghua.edu.cn

Authors

Jinqun Gan − *Ministry of Education Key Laboratory of Bioorganic Phosphorus Chemistry & Chemical Biology, Department of Chemistry, Tsinghua University, Beijing 100084, P. R. China;* orcid.org/0009-0003-8597-3855

Jiaqi Lei − *Ministry of Education Key Laboratory of Bioorganic Phosphorus Chemistry & Chemical Biology, Department of Chemistry, Tsinghua University, Beijing 100084, P. R. China*

Yongcan Li − *Ministry of Education Key Laboratory of Bioorganic Phosphorus Chemistry & Chemical Biology, Department of Chemistry, Tsinghua University, Beijing 100084, P. R. China*

Meixin Lu − *Ministry of Education Key Laboratory of Bioorganic Phosphorus Chemistry & Chemical Biology, Department of Chemistry, Tsinghua University, Beijing 100084, P. R. China*

Xinyang Yu − *Ministry of Education Key Laboratory of Bioorganic Phosphorus Chemistry & Chemical Biology, Department of Chemistry, Tsinghua University, Beijing 100084, P. R. China*

Complete contact information is available at: https://pubs.acs.org/10.1021/jacs.4c12166

Notes

The authors declare no competing financial interest.

ACKNOWLEDGMENTS

This work is supported by the National Key R&D Program of China (no. 2023YFC34031002, 2023YFE0204900), the Beijing Municipal Science & Technology Commission (no. Z231100007223007), the National Natural Science Foundation of China (no. 22175107, 22305140), and the Starry Night Science Fund of Zhejiang University Shanghai Institute for Advanced Study (SN−ZJU−SIAS−006).

REFERENCES

(1) Pardi, N.; Hogan, M. J.; Porter, F. W.; Weissman, D. mRNA vaccines - a new era in vaccinology. *Nat. Rev. Drug Discovery* **2018**, *17*, 261−279.

(2) Chaudhary, N.; Weissman, D.; Whitehead, K. A. mRNA vaccines for infectious diseases: principles, delivery and clinical translation. *Nat. Rev. Drug Discovery* **2021**, *20*, 817−838.

(3) Huang, X.; Kong, N.; Zhang, X.; Cao, Y.; Langer, R.; Tao, W. The landscape of mRNA nanomedicine. *Nat. Med.* **2022**, *28*, 2273−2287.

(4) Hou, X.; Zaks, T.; Langer, R.; Dong, Y. Lipid nanoparticles for mRNA delivery. *Nat. Rev. Mater.* **2021**, *6*, 1078−1094.

(5) Cheng, Q.; Wei, T.; Farbiak, L.; Johnson, L. T.; Dilliard, S. A.; Siegwart, D. J. Selective organ targeting (SORT) nanoparticles for tissue-specific mRNA delivery and CRISPR-Cas gene editing. *Nat. Nanotechnol.* **2020**, *15*, 313−320.
(6) Lorentzen, C. L.; Haanen, J. B.; Met, O.; Svane, I. M. Clinical advances and ongoing trials on mRNA vaccines for cancer treatment. *Lancet Oncol.* **2022**, *23*, e450−e458.
(7) Xue, L.; Gong, N.; Shepherd, S. J.; Xiong, X.; Liao, X.; Han, X.; Zhao, G.; Song, C.; Huang, X.; Zhang, H.; et al. Rational Design of Bisphosphonate Lipid-like Materials for mRNA Delivery to the Bone Microenvironment. *J. Am. Chem. Soc.* **2022**, *144*, 9926−9937.
(8) Rojas, L. A.; Sethna, Z.; Soares, K. C.; Olcese, C.; Pang, N.; Patterson, E.; Lihm, J.; Ceglia, N.; Guasp, P.; Chu, A.; et al. Personalized RNA neoantigen vaccines stimulate T cells in pancreatic cancer. *Nature* **2023**, *618*, 144−150.
(9) Swingle, K. L.; Safford, H. C.; Geisler, H. C.; Hamilton, A. G.; Thatte, A. S.; Billingsley, M. M.; Joseph, R. A.; Mrksich, K.; Padilla, M. S.; Ghalsasi, A. A.; et al. Ionizable Lipid Nanoparticles for In Vivo mRNA Delivery to the Placenta during Pregnancy. *J. Am. Chem. Soc.* **2023**, *145*, 4691−4706.
(10) Liu, C.; Shi, Q.; Huang, X.; Koo, S.; Kong, N.; Tao, W. mRNA-based cancer therapeutics. *Nat. Rev. Cancer* **2023**, *23*, 526−543.
(11) Chee, N. T.; Lohse, I.; Brothers, S. P. mRNA-to-protein translation in hypoxia. *Mol. Cancer* **2019**, *18*, No. 49.
(12) Willi, J.; Kupfer, P.; Evequoz, D.; Fernandez, G.; Katz, A.; Leumann, C.; Polacek, N. Oxidative stress damages rRNA inside the ribosome and differentially affects the catalytic center. *Nucleic Acids Res.* **2018**, *46*, 1945−1957.
(13) Jamar, N. H.; Kritsiligkou, P.; Grant, C. M. The non-stop decay mRNA surveillance pathway is required for oxidative stress tolerance. *Nucleic Acids Res.* **2017**, *45*, 6881−6893.
(14) Tal, M. C.; Sasai, M.; Lee, H. K.; Yordy, B.; Shadel, G. S.; Iwasaki, A. Absence of autophagy results in reactive oxygen species-dependent amplification of RLR signaling. *Proc. Natl. Acad. Sci. U.S.A.* **2009**, *106*, 2770−2775.
(15) Shadel, G. S.; Horvath, T. L. Mitochondrial ROS signaling in organismal homeostasis. *Cell* **2015**, *163*, 560−569.
(16) Fang, C.; Wei, X.; Wei, Y. Mitochondrial DNA in the regulation of innate immune responses. *Protein Cell* **2016**, *7*, 11−16.
(17) Willems, P. H.; Rossignol, R.; Dieteren, C. E.; Murphy, M. P.; Koopman, W. J. Redox Homeostasis and Mitochondrial Dynamics. *Cell Metab.* **2015**, *22*, 207−218.
(18) Sies, H.; Jones, D. P. Reactive oxygen species (ROS) as pleiotropic physiological signalling agents. *Nat. Rev. Mol. Cell Biol.* **2020**, *21*, 363−383.
(19) Cheung, E. C.; Vousden, K. H. The role of ROS in tumour development and progression. *Nat. Rev. Cancer* **2022**, *22*, 280−297.
(20) Koritzinsky, M.; Wouters, B. G.Hypoxia and Regulation of Messenger RNA Translation. In *Methods in Enzymology*; Elsevier, 2007; Vol. *435*, pp 247−273.
(21) Ma, Y.; Fenton, O. S. A Unified Strategy to Improve Lipid Nanoparticle Mediated mRNA Delivery Using Adenosine Triphosphate. *J. Am. Chem. Soc.* **2023**, *145*, 19800−19811.
(22) Kioka, H.; Kato, H.; Fujikawa, M.; Tsukamoto, O.; Suzuki, T.; Imamura, H.; Nakano, A.; Higo, S.; Yamazaki, S.; Matsuzaki, T.; et al. Evaluation of intramitochondrial ATP levels identifies G0/G1 switch gene 2 as a positive regulator of oxidative phosphorylation. *Proc. Natl. Acad. Sci. U.S.A.* **2014**, *111*, 273−278.
(23) Lee, P.; Chandel, N. S.; Simon, M. C. Cellular adaptation to hypoxia through hypoxia inducible factors and beyond. *Nat. Rev. Mol. Cell Biol.* **2020**, *21*, 268−283.
(24) Chang, C. C.; Dinh, T. K.; Lee, Y. A.; Wang, F. N.; Sung, Y. C.; Yu, P. L.; Chiu, S. C.; Shih, Y. C.; Wu, C. Y.; Huang, Y. D.; et al. Nanoparticle Delivery of MnO(2) and Antiangiogenic Therapy to Overcome Hypoxia-Driven Tumor Escape and Suppress Hepatocellular Carcinoma. *ACS Appl. Mater. Interfaces* **2020**, *12*, 44407−44419.
(25) Wang, C.; Guan, Y.; Lv, M.; Zhang, R.; Guo, Z.; Wei, X.; Du, X.; Yang, J.; Li, T.; Wan, Y.; et al. Manganese Increases the Sensitivity of the cGAS-STING Pathway for Double-Stranded DNA and Is Required for the Host Defense against DNA Viruses. *Immunity* **2018**, *48*, 675−687.
(26) Lv, M.; Chen, M.; Zhang, R.; Zhang, W.; Wang, C.; Zhang, Y.; Wei, X.; Guan, Y.; Liu, J.; Feng, K.; et al. Manganese is critical for antitumor immune responses via cGAS-STING and improves the efficacy of clinical immunotherapy. *Cell Res.* **2020**, *30*, 966−979.
(27) Sun, X.; Zhang, Y.; Li, J.; Park, K. S.; Han, K.; Zhou, X.; Xu, Y.; Nam, J.; Xu, J.; Shi, X.; et al. Amplifying STING activation by cyclic dinucleotide-manganese particles for local and systemic cancer metalloimmunotherapy. *Nat. Nanotechnol.* **2021**, *16*, 1260−1270.
(28) Liu, D.; Liang, S.; Ma, K.; Meng, Q. F.; Li, X.; Wei, J.; Zhou, M.; Yun, K.; Pan, Y.; Rao, L.; et al. Tumor Microenvironment-Responsive Nanoparticles Amplifying STING Signaling Pathway for Cancer Immunotherapy. *Adv. Mater.* **2024**, *36*, No. e2304845.
(29) Xu, B.; Cui, Y.; Wang, W.; Li, S.; Lyu, C.; Wang, S.; Bao, W.; Wang, H.; Qin, M.; Liu, Z.; et al. Immunomodulation-Enhanced Nanozyme-Based Tumor Catalytic Therapy. *Adv. Mater.* **2020**, *32*, No. e2003563.
(30) Zhu, Y.; Wang, W.; Cheng, J.; Qu, Y.; Dai, Y.; Liu, M.; Yu, J.; Wang, C.; Wang, H.; Wang, S.; et al. Stimuli-Responsive Manganese Single-Atom Nanozyme for Tumor Therapy via Integrated Cascade Reactions. *Angew. Chem., Int. Ed.* **2021**, *60*, 9480−9488.
(31) Gibney, G. T.; Weiner, L. M.; Atkins, M. B. Predictive biomarkers for checkpoint inhibitor-based immunotherapy. *Lancet Oncol.* **2016**, *17*, e542−e551.
(32) Jiang, X. W. J.; Wang, J.; Deng, X.; Xiong, F.; Ge, J.; Xiang, B.; Wu, X.; Ma, J.; Zhou, M.; Li, X.; Li, Y.; Li, G.; Xiong, W.; Guo, C.; Zeng, Z. Role of the Tumor Microenvironment in PD-L1/PD-1-Mediated Tumor Immune Escape. *Mol. Cancer* **2019**, *18*, No. 10.
(33) Solomon, B.; Young, R. J.; Rischin, D. Head and neck squamous cell carcinoma: Genomics and emerging biomarkers for immunomodulatory cancer treatments. *Semin. Cancer Biol.* **2018**, *52*, 228−240.
(34) Lechner, M.; Liu, J.; Masterson, L.; Fenton, T. R. HPV-associated oropharyngeal cancer: epidemiology, molecular biology and clinical management. *Nat. Rev. Clin. Oncol.* **2022**, *19*, 306−327.

https://doi.org/10.1021/jacs.4c12166
J. Am. Chem. Soc. 2024, 146, 32689−32700